Proceedings of the Combustion Institute 40 (2024) 105688

Contents lists available at ScienceDirect

Proceedings of the Combustion Institute

journal homepage: www.elsevier.com/locate/proci

3D flame surface curvature analysis from reconstructed scanning across spherical expanding flames

Yutao Zheng [a,*], Pervez Ahmed [b], Simone Hochgreb [a]

[a] University of Cambridge, Engineering Department, Trumpington St, Cambridge, CB2 1PZ, United Kingdom
[b] University of Leeds, Engineering Department, Woodhouse Ln., Woodhouse, Leeds, LS2 9JT, United Kingdom

ARTICLE INFO

Keywords:
Principal curvatures
Spherical expanding flames
Scanning reconstruction

ABSTRACT

We analyze 3D reconstructed surfaces based on previously reported high frequency measurements of flame edge location across expanding flames using Mie scatter. For the first time, principal curvatures of flame surfaces are estimated from eigenvalues of the second fundamental forms of the reconstructed surfaces, allowing the determination of the statistics of mean and Gaussian curvatures as a function of time and thus flame mean radius. Measurements and analysis were made for both lean methane and hydrogen mixtures as a function of time and turbulence levels. The mean 3D flame curvature was found to be inversely proportional to flame radius, and relatively insensitive to turbulence intensity, even in the case of larger, more planar flames. Mean 3D curvatures across the flame brush were determined to be positive (convex) towards the reactant mixture at the leading edge, and negative (concave) towards the trailing edge, as predicted from DNS measurements. The mean and probability distributions of 3D mean curvatures were found to be significantly different than 2D curvatures extracted from the central planes, with the 3D measurements showing much narrower distributions and lower values. Differences between 3D and 2D measurements were different by an order of magnitude in the case of hydrogen flames, possibly owing to the onset of thermodiffusive instabilities which affect the local fine structure of the flame.

1. Introduction

Spherical expanding flames have been extensively investigated as a method for studying turbulent flame propagation in isotropic turbulence. Previous experimental investigations have primarily used 2D imaging techniques to extract flame surface contours, employing either Mie scattering across the central plane [1] or line-of-sight schlieren techniques [2,3].

Previous extraction of 3D surface properties have been based on tomographic imaging [4–9], and reconstruction of based on 2D scanned images [10–13]. Properties of interest are typically flame curvature, orientation and surface density. In particular, 3D flame surface curvature can play a role and correlate with local heat release rate [14,15] and flame surface propagation [16].

To date, 3D curvature measurements of turbulent combustion have been based on tomographic [7,17] or scanning techniques [18]. Yu et al. [7] employed nine projection views to capture the chemiluminescence of a swirl flame and reconstructed instantaneous flame profiles. The horizontal and vertical spatial resolutions were estimated to be of the order of 0.41 mm and 1 mm, respectively, enabling the resolution of 3D curvatures under 1 mm^{-1}. Using a similar technique, Ma et al. [17] applied a three-point finite-differencing scheme with six CMOS cameras to evaluate 2D flame curvatures and further estimated the 3D Gaussian curvature using a fixed orthogonal coordinate in a slot Bunsen flame.

In a study based on a quasi-volumetric laser illumination scanning technique, Li et al. [18,19] reconstructed the instantaneous turbulent jet flame surface. Flame surface stretch rates were obtained by estimating 3D principal curvatures and local velocities, and the joint PDF of mean and Gaussian curvature were plotted to illustrate 3D flame surface stretch rate in the flame brush.

Yet so far, there have been no determinations of 3D curvature in expanding spherical flames. Given the significant correlations found between flame propagation and curvature, especially in the case of hydrogen mixtures [20], it is important to characterize the true 3D curvatures, and to understand how the mean and deviation of ubiquitous 2D curvature measurements truly represent (or not) the real flame curvature.

The present study is based on the 3D scanning measurements of spherically expanding flames described by Ahmed et al. [21]. The investigation covers experiments involving methane/air flame and hydrogen/air mixtures. The analysis includes determination of the statistical

* Corresponding author.
E-mail address: yz615@cam.ac.uk (Y. Zheng).

https://doi.org/10.1016/j.proci.2024.105688
Received 3 December 2023; Accepted 25 July 2024
Available online 5 August 2024

properties of principal, mean, and Gaussian curvatures as a function of time and flame radius and position in the flame brush, for different mixtures and turbulent intensity values.

2. Methodology

The details of the experimental setup are detailed in the original publication [21], while a summary is offered here for context.

2.1. Experimental setup

Premixed turbulent spherical flames were ignited in a spherical combustion vessel with an internal diameter of 380 mm, featuring three pairs of orthogonal windows each with a diameter of 150 mm for optical access [21]. The initial mixture temperatures and static pressures were measured using a K-type thermocouple and a static pressure sensor, respectively [22]. Turbulence in the central region of the combustion vessel was generated by four fans, and the corresponding turbulent rms velocity and integral length scales were determined in previous studies using laser Doppler anemometry [22,23].

Olive oil droplets, with a density of 970 $\mathrm{kg/m^3}$ and an approximate size of 1 μm, served as seeding particles for the 2D Mie scattering images. The droplets evaporate at temperatures ranging from 600 to 700 K, providing a flame edge detected at a normalized isotherm corresponding to a progress of reaction $c^* = 0.2{\sim}0.3$ in this study.

The swinging laser sheet technique employed a double-cavity 532 nm Nd:YAG laser for Mie-scatter flame imaging, pulsing at a frequency of 54 kHz with a pulse energy of about 1.9 mJ. A total of 78 laser sheets (thickness of ∼0.6 mm) per sweep are created using a 16-faced mirror rotating at 12 Hz [21]. The sheets were separated by approximately 1 mm and 18 μs. Reflected light from a diode laser pointing to another face of the multi-faced rotating mirror was captured by a photodiode detector as a calibration to synchronize the laser and the scanning location and served as a surrogate for reproducibility [24]. The time interval between the first and last sheet images recorded (sweep duration), was 1.44 ms. The time interval between two successive sweeps was 5.2 ms.

A high-speed Phantom VR camera, placed orthogonally to the imaging laser sheets, captured 2D Mie-scattered images using a fixed macro lens with a focal length of 105 mm at every position of the laser sheet. A minimum aperture with a large focal number of $f/32$ was used to generate a sufficiently large depth of field to cover the entire flame volume. These images were taken with an exposure of 6 μs at a resolution of 512 × 512 pixels. The spatial resolution was measured in three different planes. The center plane resolution was recorded as 0.196 mm/pixel while for the nearest and the farthest plane the results were 0.1827 mm/pixel and 0.2095 mm/pixel [24], respectively. A linear interpolation was used for the intermediate resolutions. The resolution around 0.2 mm is sufficiently small to resolve the Taylor length scale (which varied between 1.2–2.6 mm) but not the Kolmogorov scale (which varied between 0.03–0.12 mm).

2.2. 3D flame surface reconstruction

Multiple flame surface contours, extracted from 2D Mie scattering images were used to reconstruct instantaneous 3D flame surfaces using Matlab subroutines. A post-processing step is necessary to match the resolutions of the imaging plane (0.2 mm) and the corresponding orthogonal plane (1 mm), here accomplished by filtering down to the lower resolution. A filter (here using MATLAB function `imresize`) equal to the larger spatial dimension of 1 mm is used to smooth flame contours on each projected image. The coordinates corresponding to the location of the Mie-scatter 2D iso-surfaces at different planes were used as inputs to the `isosurface` command, producing a list of coordinates corresponding to the locations of iso-values for the surface.

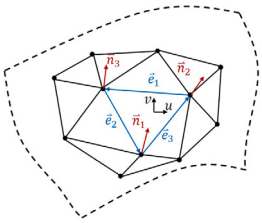

Fig. 1. Representative 3D triangle mesh with three edge vectors and three normal vectors attached to the vertices [28].

The `patch` command used the list of coordinates to generate a surface mesh of triangular faces, linked by vertices at the coordinates. To preserve the surface features of the reconstruction while minimizing shrinkage, a smoothing algorithm described by Taubin et al. [25] was adopted to move vertices of triangulated surfaces without changing the connectivity of the faces [26]. The processed surface contains exactly the same number of faces and vertices as the original version defined by the command `patch`.

The triangular face areas A are calculated from the location of vertex coordinates using Heron's formula,[1] and the volume V_b is calculated by integrating the volume ratio of product within a radius as $V_b = 4\pi \int_0^\infty \bar{c}(r) r^2 \, dr$, where $\bar{c}(r)$ is the circumferentially averaged local probability of finding product [27]. The product area is estimated by calculating the intersection between the r-sphere and reconstruct triangles on each volume element and estimating the contribution on area.

The burned gas equivalent radius can then be determined as $R_v = \left(\frac{3}{4\pi} V_b\right)^{1/3}$. The mean surface location can be reconstructed from the probability of finding burned gas at a given flame radius, $c(\mathbf{r}, t)$, as mean progress of reaction $\bar{c} = \frac{1}{V} \int_{\mathcal{V}} c(\mathbf{r}, t) \, dV$. The flame brush corresponds to the region between $\bar{c} = 1$ (trailing edge) and $\bar{c} = 0$ (leading edge) [1,3].

2.3. Determination of curvature

The method of Rusinkiewicz was chosen to determine the normal vector and principal curvatures based on *irregular triangular* surface meshes [28]. Fig. 1 shows an illustration of three vectors ($\mathbf{e_1}$, $\mathbf{e_2}$, $\mathbf{e_3}$) forming a triangle mesh and normal vectors at vertices ($\mathbf{n_1}$, $\mathbf{n_2}$, $\mathbf{n_3}$).

The curvatures are determined as the eigenvalues of the second fundamental tensor **II** representing the spatial gradient of the normal vectors. Normal vectors associated with the vertices $\mathbf{n_i}$ ($i = 1, 2, 3$) are derived from the weighted-average of normal vectors of adjacent triangle faces $\mathbf{n_f}$ [29].

$$\mathbf{n}_i = \sum_f w_{i,f} \mathbf{n}_{i,f} \tag{1}$$

where $\mathbf{n}_{i,f}$ are normal vectors of the triangle faces that touch the vertex i; the weight coefficients $w_{i,f}$ correspond to the area of the triangle divided by the squares of the length of the two edges that touch the vertex [7].

The second fundamental tensor II is defined in terms of directional derivatives of the surface normal:

$$\mathrm{II} = \begin{bmatrix} D_u \mathbf{n} & D_v \mathbf{n} \end{bmatrix} = \begin{bmatrix} \frac{\partial \mathbf{n}}{\partial \mathbf{u}} \cdot \mathbf{u} & \frac{\partial \mathbf{n}}{\partial \mathbf{v}} \cdot \mathbf{u} \\ \frac{\partial \mathbf{n}}{\partial \mathbf{u}} \cdot \mathbf{v} & \frac{\partial \mathbf{n}}{\partial \mathbf{v}} \cdot \mathbf{v} \end{bmatrix} \tag{2}$$

In the triangle mesh coordinate system, the tensor matrix elements for the relevant normal gradient can be written as follows:

$$\mathbf{M}_i = \mathrm{II} \begin{bmatrix} \mathbf{e_i} \cdot \mathbf{u} \\ \mathbf{e_i} \cdot \mathbf{v} \end{bmatrix} = \mathrm{II} \begin{bmatrix} (\mathbf{n_k} - \mathbf{n_j}) \cdot \mathbf{u} \\ (\mathbf{n_k} - \mathbf{n_j}) \cdot \mathbf{v} \end{bmatrix} \tag{3}$$

[1] Heron's formula $A = \sqrt{p(p-a)(p-b)(p-c)}$, where a, b, and c are the lengths of the triangle, and p is the perimeter.

Fig. 2. Schematic diagram for three types of surfaces.

Table 1
Experimental cases considered in [21].

Num	CH_4	H_2
Φ	0.7	0.3
u' (m/s)	0.3–1.5	0.3-1.5
P (MPa)	0.1	0.5
P_f (MPa)	0.66	1.75
T (K)	300	365
s_L (m/s)	0.210	0.102
$\tau = \rho_u/\rho_b$	6.09	3.19
$K = \mathrm{Ka}/\sqrt{15}$	0.027–0.30	0.049-0.85
Le	1.0	0.3 [32,33]
Ma	2.7	−5.0

where $\mathbf{e}_1$, $\mathbf{e}_2$, and $\mathbf{e}_3$ are three edge vectors of the triangle, and $\mathbf{n}_1$, $\mathbf{n}_2$ and $\mathbf{n}_3$ are the normal vectors attached to the respective vertices.

Principal curvatures at each vertex i are finally evaluated from the determination of the two eigenvalues $\kappa_1 \geq \kappa_2$ of $\mathbf{M}_i$, realized via a least squares method. In this study, positive curvatures correspond to the center of curvature inside the product side (convex to the reactant side). The resolution of principal curvatures is limited by larger of the values between the spatial resolution across the imaging plane ($\Delta_{2D} = 0.2$ mm) and orthogonal direction between planes ($d_s = 1$ mm) [13].

The mean curvature κ_m and Gaussian curvature κ_g are derived from principal curvatures, according to:

$$\kappa_m = \frac{\kappa_1 + \kappa_2}{2} \tag{4}$$

$$\kappa_g = \kappa_1 \kappa_2 \leq \left(\frac{\kappa_1 + \kappa_2}{2}\right) = \kappa_m^2 \tag{5}$$

Based on the sign of the Gaussian curvature, surface structures can be categorized as elliptical ($\kappa_g > 0$), cylindrical ($\kappa_g = 0$) and hyperboloid ($\kappa_g < 0$), as illustrated in Fig. 2.

The largest resolution in-plane (Δ_{2D}) and orthogonal plane directions (d_s) define the cut-off of large principal curvature to $\kappa_1, \kappa_2 > 1\ \mathrm{mm}^{-1}$.

The 2D curvature κ_{2D} is extracted from 2D projected flame contours on the central plane, defined as $\kappa_{2D} = (x'y'' - x''y')(x'^2 + y'^2)^{-3/2}$, where $\mathbf{x} = (x(s), y(s))$ represents the two-dimensional parametric curve describing the flame location, and where prime and double prime represent the first and second derivative with respect to the flame length parameter s. The pixel resolution of the 2D images is limited to 0.196 mm, resulting in a low-pass cut-off of 2D curvatures $\kappa_{2D} > 5\ \mathrm{mm}^{-1}$. The 2D curvatures κ_{2D} offer a larger dynamic range, but cannot represent the flame surface wrinkling in the third direction.

2.4. Experimental cases

Turbulent mixtures of air with methane or hydrogen were considered in [21], as listed on Table 1 along with measured and calculated parameters. Results were repeated three times, and all 6 results for the two cases presented were analyzed to obtain the relevant statistics. The original paper describes how the relevant properties and parameters were obtained. Laminar flame speeds and equilibrium temperatures were calculated using Cantera 2.5.1 [30] and GRI Mech 3.0 [31].The integral length scale measured was $L = 20$ mm.

Mixtures were chosen based on the relatively low burning rates, so as to be accessible to the optical diagnostic technique sweep times. A key difference between the mixtures is the different sign of the Markstein number: positive for CH_4 and negative for H_2. The sign of $\mathrm{Ma} \propto (\mathrm{Le} - 1)$ and is related to the propensity for instabilities [1,34]: lean hydrogen flames are significantly more prone to thermodiffusive instabilities, unlike lean methane flames.

3. Results

3.1. 3D curvatures

Fig. 3 shows the flame surface expansion for a methane mixture at a low turbulence intensity of $u' = 0.3$ m/s. The flame surfaces maintain mean spherical geometry in general, as the local flame surface is wrinkled by turbulence. As the flame ball expands from a volume corresponding to burned gas radius $R_v = 8.0$ mm ($t = 5.91$ ms) to $R_v = 24.3$ mm ($t = 11.12$ ms), flame surface structures develop over a range of scales. For example, the small bump in Fig. 3(c) develops into a local peak in Fig. 3(d) highlighted by black rectangles.

Fig. 4 shows principal curvatures, κ_1 and κ_2, mean curvature, κ_m, and Gaussian curvature, κ_g in the methane case at $t = 21.54$ ms, corresponding to Fig. 3(d). A black dashed-line region is magnified to highlight different surface features, as the eigenvalues of matrix $\mathbf{M}$, principal curvatures $\kappa_1 > \kappa_2$ represent the local maximum and minimum 2D curvatures at two orthogonal projected planes intersecting at the local normal vector ($\kappa_1 > \kappa_2$), and the magnitudes of κ_m and κ_g represent the level of flame surface wrinkling. The joint PDFs of the two principal curvatures are plotted in Fig. 5 for the latest observed time, when the flames are sufficiently large to provide converged PDFs ($t = 31.95$ ms). The peak PDF values appear near zero curvature, with a slightly positive mean.

The results for Gaussian and mean curvature are collected and represented as a joint PDF across the whole flame in Fig. 6 for $t = 31.95$ ms. The parabolic boundary reflects the constraint of $\kappa_g \leq \kappa_m^2$ in Eq. (5) [7]. Red regions represent a higher probability. Small scale flame surface structures located in the first and fourth quadrant for positive mean curvatures. Fig. 6 also shows that there are more points deviating from the parabolic limit in the hydrogen flame than the methane flame, shown by its thicker red region. Such a deviation can be characterized by the difference of two principal curvatures, $\kappa_1 - \kappa_2$ as follows.

Fig. 7 shows the PDFs of $\kappa_1 - \kappa_2$, where positive or negative values refer to dominant elliptical or hyperboloid surfaces as determined by the sign of κ_g. The transition near zero represents surfaces with nearly equal principal curvatures. The figure shows that apparently, there are larger fractions of elliptical than hyperboloid surfaces, and that as the flame ball expands, the proportion of elliptical surfaces reduces while the proportion of hyperboloid surfaces holds relatively steady in both methane and hydrogen flames.

Since κ_1 and κ_2 represent the maximum and minimum of 2D projected curvatures, respectively, any 2D projected curvatures κ_{2D} are the range of $[\kappa_2, \kappa_1]$. When $\kappa_1 - \kappa_2 = 0$, flame surfaces are elliptical and we should expect $\kappa_2 = \kappa_{2D} = \kappa_1$. Therefore, for these types of surfaces, local 3D flame surfaces areas can be estimated by 2D projected flame contours.

For $\kappa_1 - \kappa_2 > 0$, the value κ_{2D} is within $[\kappa_2, \kappa_1]$. For larger values of the difference $\kappa_1 - \kappa_2$, the difference between the 3D and 2D values of curvature becomes larger. The range of $\kappa_1 - \kappa_2$ is wider for hydrogen than methane mixtures, in both the elliptical and hyperboloid side, implying that the possible discrepancy between κ_{2D} and κ_m should be higher in the hydrogen than the methane case. On the right side of Fig. 7 where $\kappa_g > 0$, two principal curvatures have the same sign and the one curvature with a larger magnitude would be closer to the cut-off curvature at 1 mm^{-1}. The hydrogen curvatures extend closer to the limit and show that hydrogen flames would have more flame surface structures filtered by the spacing of the scanning technique, as illustrated by the limits indicated by dashed lines in Fig. 5.

Fig. 8 shows the evolution of PDFs of κ_m and κ_g for both mixtures with $u' = 0.3$ m/s, along with 2D PDFs for the later time $t = 31.95$ ms.

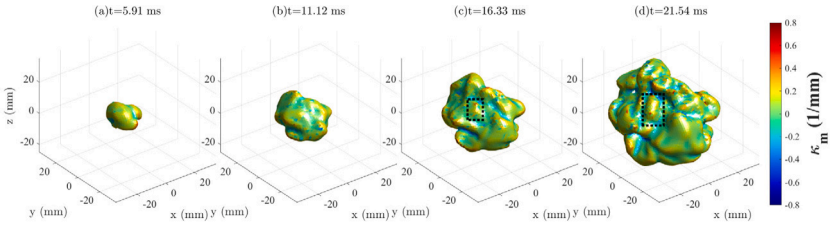

Fig. 3. Time sequence for methane–air expanding flame surface from t = 5.91 ms to t = 21.54 ms, for u' = 0.3 m/s, colored by mean curvature, κ_m. (For interpretation of the references to color in this figure legend, the reader is referred to the web version of this article.)

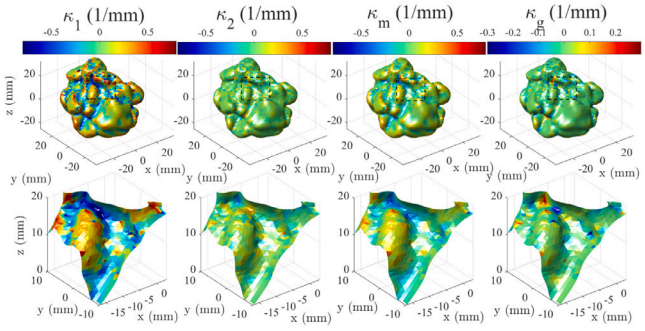

Fig. 4. Principal, mean and Gaussian curvatures obtained for CH4/air flames at t = 21.54 ms. Upper row: entire flame surfaces colored by respective curvatures; bottom row: magnified region corresponding to the black-dashed region in the upper row. (For interpretation of the references to color in this figure legend, the reader is referred to the web version of this article.)

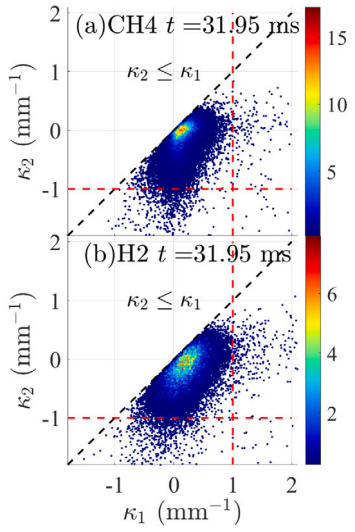

Fig. 5. Joint-PDF for two principal curvatures, κ_1 and κ_2 for the late snapshot for methane and hydrogen flames (u' = 0.3 m/s). Black dash line: the limit of $\kappa_2 \leq \kappa_2$; red dashed lines represent the estimated limits of spatial resolution, 1 mm^{-1}. (For interpretation of the references to color in this figure legend, the reader is referred to the web version of this article.)

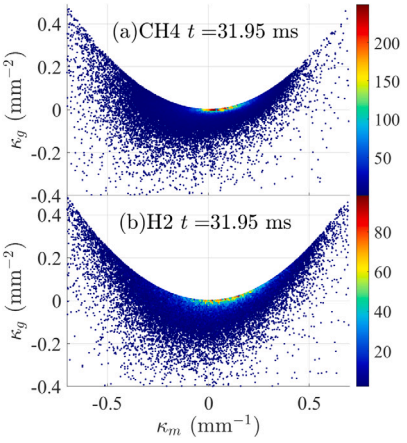

Fig. 6. Joint-PDF for the mean curvature κ_m and the Gaussian curvature κ_g for the late snapshot of methane and hydrogen flames (u' = 0.3 m/s).

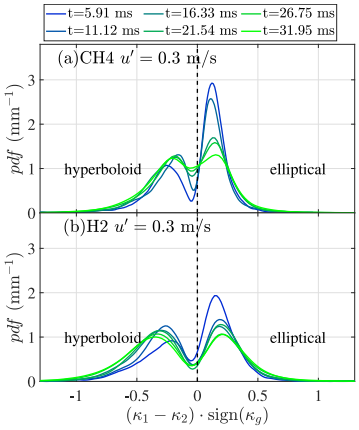

Fig. 7. PDFs of the difference of two principal curvatures $\kappa_1 - \kappa_2$ conditional on the sign of κ_g.

The early 2D data include only a limited number of points, and cannot provide a converged PDF of 2D curvature κ_{2D}. The distributions of 3D κ_m broaden as a function of time, as a larger fraction of the surface regions with high curvature emerges. The mode of κ_m moves to the left over time, although the mean is still positive, whilst hydrogen mixtures show a more pronounced negative tail than methane. The Gaussian curvature mode is slightly positive, and largely symmetric, whilst spreading at later times. The increasing symmetry of the profiles as a function of time indicate a greater equilibrium of structures across a more isotropic flame, even though the mean curvature may be skewed. Note that in general, only a small fraction of the structures appears to extend beyond 1 mm^{-1}, where the current experimental spatial resolution necessarily filters the distribution.

The dashed lines on the left column of Fig. 8 represent the PDF of 2D curvatures measured along the central imaging plane (CIP), whilst the dotted lines correspond to the corresponding orthogonal central imaging plane (OCIP), obtained by interpolating across images at the lower resolution, both at t = 31.95 ms, which can be compared to the light green solid line curves for κ_m. The 2D PDF distributions on the CIP with the pixel resolution of ≈ 0.2 mm are slightly wider than the PDFs on the OCIP for which the resolution is 1 mm. The discrepancy between the dashed and dotted lines represents the proportion of flame contours where the radius of 2D curvatures are in the range of 0.2~1 mm, which is filtered in the OCIP. It is not clear why the distribution for

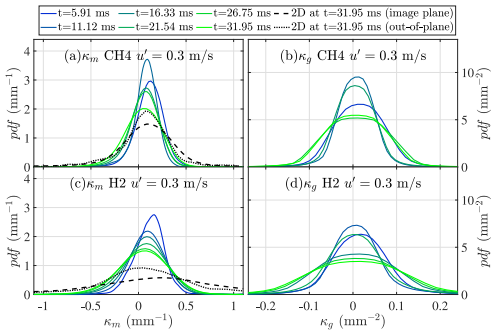

Fig. 8. PDFs of mean curvatures κ_m (left) and Gaussian curvature κ_g (right) as a function of time for two mixtures at a given turbulence level. Blue–green solid lines: 3D curvatures time sequence color key follows that of Fig. 7. Black dashed and dotted lines: 2D curvatures extracted from flame contours across the central imaging plane (dashed) and cross-imaging plane (dotted), both determined at $t = 31.95$ ms. (For interpretation of the references to color in this figure legend, the reader is referred to the web version of this article.)

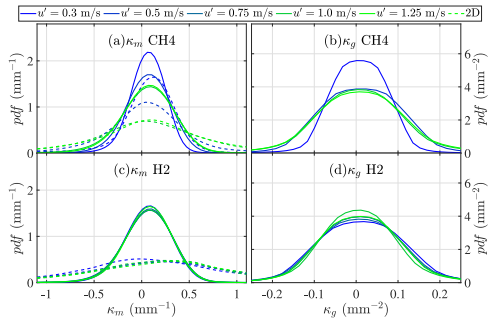

Fig. 9. PDFs of mean curvatures κ_m (top) and Gaussian curvature (bottom) κ_g under different turbulence intensity for the two mixtures, for a range of mean flame radius between 16–20 mm. Blue–green solid lines: 3D curvatures from low to high turbulence. Dashed lines: 2D curvatures. (For interpretation of the references to color in this figure legend, the reader is referred to the web version of this article.)

the CIP appears skewed towards positive curvatures in both methane and hydrogen cases. 2D PDF distributions are also clearly significantly wider than the 3D measurements, even though the resolution is 1 mm for both 3D mean curvatures and 2D curvatures on the OCIP. There are two potential reasons for the difference. On one hand, a wide distribution can be clipped by the filter, as discussed above. This is only relevant in the case of hydrogen, which is somewhat more widely spread than the case of methane. More likely, the difference between 2D and 3D reflects the prevalence of structures for which $|\kappa_1 - \kappa_2|$ is non-zero, as discussed in Fig. 7. For these cases, the projection of the curvature on a 2D plane would be captured as contributing to a larger curvature. This is more prominent in the hydrogen case, where the discrepancy between 3D curvatures (green) and 2D curvatures on the orthogonal plane (dotted) is not negligible. This is consistent with the wider distribution of hyperboloid surfaces in Fig. 7, leading to more frequent principal curvature differences $\kappa_1 - \kappa_2$ in the case of hydrogen flames.

Fig. 9 shows the PDF distribution of mean and Gaussian curvatures for varying different turbulence intensities, for a point in time where volumetric equivalent radius, R_v, is fixed in the range of 16 mm to 20 mm . The PDFs of κ_m and κ_g become broader as u' increases in methane flames, but there are negligible changes for hydrogen flames. Again, 2D curvatures κ_{2D} are shown for comparison with mean curvatures κ_m, showing a similarly large discrepancy level between the 3D κ_m and κ_{2D}, as shown in Fig. 8. Fig. 9 also shows that the PDF of mean and Gaussian curvatures changes little for turbulence intensities beyond 0.5 m/s in the case of methane, and for all intensities in the case of hydrogen. This low dependence is striking, particularly in the case of hydrogen.

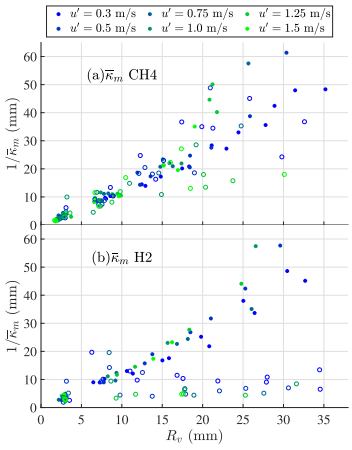

Fig. 10. Reciprocal curvature $1/\bar{\kappa}_m$ vs. R_v for a range of turbulence intensities u'. Open symbols: 2D.

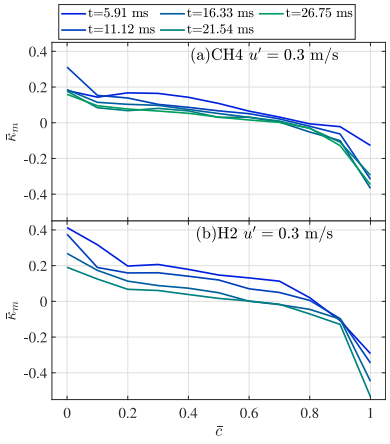

Fig. 11. Mean curvatures $\bar{\kappa}_m(\bar{c})$ conditioned on the local $\bar{c}$ as the turbulent flame expands. (a): CH_4/air; (b): H_2/air.

We conclude from the dependence on time/radius and turbulence that the former has a stronger influence on the PDF distribution of flame surface curvatures than turbulence itself. A detailed uncertainty analysis is presented in Appendix.

Fig. 10 shows how the reciprocal global mean curvature κ_m varies with the burned gas radius for different turbulence intensities. For small values of R_v, there is a strong linear correlation between reciprocal mean curvature and R_v, with similar slope of around 1:1 for both cases, with little effect of turbulence, particularly in the case of methane. For larger values of the flame radius, the correlation becomes weaker, with no discernible systematic effect of turbulence intensity. Notably, in the case of hydrogen mixtures (and unlike the case of methane), the reciprocal mean 2D curvatures are significantly lower than the 3D mean curvatures, which means that the 2D values are overestimated relatively to 3D. The strong influence of flame radius suggests that the isotropic expansion of the gas is the leading term.

3.2. Role of mean progress of reaction, $\bar{c}$

Fig. 11 shows the average of mean curvature κ_m across the flame brush. Flame surfaces are wrinkled into the reactant side with positive mean curvatures towards the leading edge and with negative mean curvatures for the gas towards the trailing edge. The linear correlation

between $\bar{c}$ and the conditional mean curvatures in the middle of the flame brush are consistent with other experiments using 2D curvatures [13,35,36].[2] In spherical expanding flames, the intersection of conditional mean curvatures $\bar{\kappa}_m$ with the x-axis occurs within the range of $\bar{c} = 0.6{\sim}0.8$, whereas in Bunsen flames, $\bar{\kappa}_m(\bar{c}) = 0$ at $\bar{c} = 0.3{\sim}0.4$ [13].

Fig. 11 also shows that the conditional mean curvature $\bar{\kappa}_m(\bar{c})$ decreases as the flame expands, much more so in hydrogen flames compared with methane. Finally, a study of the conditional mean curvatures for different turbulence intensity levels showed no significant difference in the profile of $\bar{\kappa}_m(\bar{c})$ for different u', a finding consistent with the constant average of κ_m in Fig. 9 and Fig. 10.

4. Conclusions

The study for the first time quantifies the distribution and mean values of 3D curvatures in a spherically expanding flame, using surfaces extracted using a scanning technique. Principal curvatures were calculated from the eigenvalues of the second fundamental spatial tensor of the local surface, allowing true mean and Gaussian curvatures to be determined. PDFs and joint PDFs of principal curvatures, mean curvatures κ_m and Gaussian curvatures κ_g were also analyzed over time sequences and across the flame brush.

It is clear that the PDF and moments of mean values of 3D curvature distributions are very different from 2D distributions. Importantly, it is shown for the first time how the reciprocal mean curvatures $1/\overline{\kappa}_m$ correlate linearly with the equivalent burned gas radius, with a minimum role of turbulence levels. The 3D mean curvatures are also shown to be positive towards the leading edge of the flames, and negative towards the trailing edge, as also found in 3D DNS [35].

Further advances in laser and imaging technology, such as higher imaging recording rates with closer spacing between sheets would enhance the quality of the resolution and expand the maximum curvature filter to enhance the investigation of mixtures exhibiting small scale instabilities, such as the case with lean hydrogen.

Novelty and significance statement

For the first time measurements of 3D flame curvature distributions are made in spherically expanding flames of methane and hydrogen. Comparisons made with usual measurements of 2D curvature distributions show very large differences in mean and probability distributions. 3D curvatures are significantly correlated with reaction rate in flames, particularly when affected by with thermodiffusive instabilities according to DNS. The measurement of the true 3D curvatures and their differences with 2D curvatures may change conclusions obtained from prior 2D measurements.

CRediT authorship contribution statement

Yutao Zheng: Conceptualization, Methodology, Data curation, Original draft, Review editing. **Pervez Ahmed:** Methodology, Data curation, Experimental investigation. **Simone Hochgreb:** Conceptualization, Original draft, Review editing.

Declaration of competing interest

The authors declare that they have no known competing financial interests or personal relationships that could have appeared to influence the work reported in this paper.

[2] Conditional averages of 2D $\kappa_{2D}(\bar{c})$ are not well converged and thus not compared with κ_m in Fig. 11.

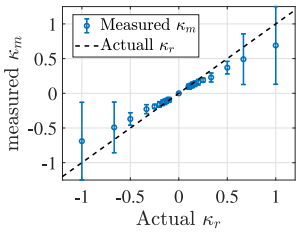

Fig. 12. Measured mean curvatures κ_m vs. actual mean curvatures κ_r. κ_m is measured from the reconstructed surface on a sphere with a known radius using the above reconstruction algorithm and the curvature estimation method.

Acknowledgments

YZ is partially supported by EPSRC EP/T015845/1. The authors are grateful to M. Lawes and D. Bradley, who supervised the original work producing the data for the present analysis. PA would like to thank University of Leeds for a research scholarship award (LIRS).

Appendix. Uncertainty analysis

The uncertainty in surface curvatures comes from: (a) random error in the location and discretization of the flame surface, and its propagation to the eigenvalues of the vector matrix and (b) systematic error from the limited resolution of the reconstruction method.

A.1. Random error

The relative uncertainty in pixel location is approximated as: $\sigma_v \approx \sqrt{2}\sigma/n = 0.28$, where σ has the length of one pixel (≈ 0.2 mm) and n is the averaged vector length, which can be estimated as the scanning distance of 1 mm.

The propagating error in deriving the eigenvalues is approximated by the condition number of eigenvalue derivations using the MATLAB function *condeig*. For most matrices, the condition number is close to 1, so that error in the vector differentiation is neither amplified or suppressed. Here we assume the relative uncertainty in final curvatures is equal to the relative uncertainty of the pixel location above.

A.2. Systematic error

The limited resolution in one direction leads to a skewness in the estimated uncertainty of real curvatures κ_r. In order to estimate the skewness, we use a series of hypothetical spheres with given radii as a target to apply the reconstruction method and measure κ_m with a given real curvature κ_r.

Fig. 12 presents the measured mean curvatures κ_m on a sphere with a given radius, given a real curvature κ_r. The blue points are the ensemble average of measured curvatures κ_m. where the error bar represents the uncertainty in κ_m for a given κ_r. The black dashed line is the real κ_r. An underestimation (29%) of κ_r when directly using κ_m can be found as the discrepancy between blue points and black dashed lines.

A.3. Uncertainty in mean curvatures

Fig. 13 shows the estimated uncertainties of the pdf of mean curvatures κ_m, and estimated real mean curvatures κ_r by adding the correction factor of 1.29 to κ_m, estimated from Fig. 12. Solid lines with error bars represent the measured κ_m where *only* the random error is considered. Black error bars on κ_m show that the random error has a negligible statistical effect on PDFs of mean curvatures κ_m. Dashed lines represents the deduced PDFs of real κ_r.

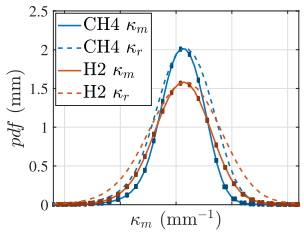

Fig. 13. PDFs of mean curvatures κ_m (solid lines) at t = 31.95 ms, compared with estimated real curvatures κ_r (dashed lines). Uncertainties of κ_m (dark blue) and κ_r (dark red) are presented as the error bar. (For interpretation of the references to color in this figure legend, the reader is referred to the web version of this article.)

References

[1] D. Bradley, M. Haq, R. Hicks, T. Kitagawa, M. Lawes, C. Sheppard, R. Woolley, Turbulent burning velocity, burned gas distribution, and associated flame surface definition, Combust. Flame 133 (2003) 415–430.

[2] S. Chaudhuri, F. Wu, D. Zhu, C.K. Law, Flame speed and self-similar propagation of expanding turbulent premixed flames, Phys. Rev. Lett. 108 (2012) 044503.

[3] D. Bradley, M. Lawes, M. Mansour, Correlation of turbulent burning velocities of ethanol-air, measured in a fan-stirred bomb up to 1.2 MPa, Combust. Flame 158 (2011) 123–138.

[4] E. Kristensson, Z. Li, E. Berrocal, M. Richter, M. Aldén, Instantaneous 3D imaging of flame species using coded laser illumination, Proc. Combust. Inst. 36 (2017) 4585–4591.

[5] J. Floyd, P. Geipel, A. Kempf, Computed tomography of chemiluminescence (CTC): instantaneous 3D measurements and phantom studies of a turbulent opposed jet flame, Combust. Flame 158 (2011) 376–391.

[6] N.A. Worth, J.R. Dawson, Tomographic reconstruction of OH* chemiluminescence in two interacting turbulent flames, Meas. Sci. Technol. 24 (2012) 024013.

[7] T. Yu, Q. Wang, C. Ruan, F. Chen, W. Cai, X. Lu, M. Klein, A quantitative evaluation method of 3D flame curvature from reconstructed flame structure, Exp. Fluids 61 (2020) 1–13.

[8] T. Upton, D. Verhoeven, D. Hudgins, High-resolution computed tomography of a turbulent reacting flow, Exp. Fluids 50 (2011) 125–134.

[9] L. Ma, Q. Lei, J. Ikeda, W. Xu, Y. Wu, C.D. Carter, Single-shot 3D flame diagnostic based on volumetric laser induced fluorescence (VLIF), Proc. Combust. Inst. 36 (2017) 4575–4583.

[10] K.Y. Cho, A. Satija, T.L. Pourpoint, S.F. Son, R.P. Lucht, High-repetition-rate three-dimensional OH imaging using scanned planar laser-induced fluorescence system for multiphase combustion, Appl. Opt. 53 (2014) 316–326.

[11] J. Weinkauff, M. Greifenstein, A. Dreizler, B. Böhm, Time resolved three-dimensional flamebase imaging of a lifted jet flame by laser scanning, Meas. Sci. Technol. 26 (2015) 105201.

[12] G. Römer, P. Bechtold, Electro-optic and acousto-optic laser beam scanners, Phys. Procedia 56 (2014) 29–39.

[13] Y. Zheng, L. Weller, S. Hochgreb, 3D flame surface measurements in low-turbulence Bunsen flames via scanning and orthogonal cross-planar techniques, Combust. Flame 258 (2023) 113103.

[14] H. Kosaka, F. Zentgraf, A. Scholtissek, C. Hasse, A. Dreizler, Effect of flame-wall interaction on local heat release of methane and DME combustion in a side-wall quenching geometry, Flow Turbul. Combust. 104 (2020) 1029–1046.

[15] A. Aspden, M. Day, J. Bell, Three-dimensional direct numerical simulation of turbulent lean premixed methane combustion with detailed kinetics, Combust. Flame 166 (2016) 266–283.

[16] M. Tsuchimoto, O. Fujita, T. Honko, Y. Nakamura, H. Ito, Research on the relation of flame front curvature and oscillatory flame propagation by external laser irradiation method, Proc. Combust. Inst. 32 (1) (2009) 1003–1009.

[17] L. Ma, Y. Wu, Q. Lei, W. Xu, C.D. Carter, 3D flame topography and curvature measurements at 5 kHz on a premixed turbulent Bunsen flame, Combust. Flame 166 (2016) 66–75.

[18] T. Li, J. Pareja, L. Becker, W. Heddrich, A. Dreizler, B. Böhm, Quasi-4D laser diagnostics using an acousto-optic deflector scanning system, Appl. Phys. B 123 (2017) 78.

[19] T. Li, B. Zhou, J.H. Frank, A. Dreizler, B. Böhm, High-speed volumetric imaging of formaldehyde in a lifted turbulent jet flame using an acousto-optic deflector, Exp. Fluids 61 (2020) 1–14.

[20] T. Howarth, E. Hunt, A. Aspden, Thermodiffusively-unstable lean premixed hydrogen flames: Phenomenology, empirical modelling, and thermal leading points, Combust. Flame 253 (2023) 112811.

[21] P. Ahmed, B. Thorne, M. Lawes, S. Hochgreb, G.V. Nivarti, R.S. Cant, Three dimensional measurements of surface areas and burning velocities of turbulent spherical flames, Combust. Flame 233 (2021) 111586.

[22] M. Lawes, M.P. Ormsby, C.G. Sheppard, R. Woolley, The turbulent burning velocity of iso-octane/air mixtures, Combust. Flame 159 (5) (2012) 1949–1959.

[23] I. Nwagwe, H. Weller, G. Tabor, A. Gosman, M. Lawes, C. Sheppard, R. Wooley, Measurements and large eddy simulations of turbulent premixed flame kernel growth, Proc. Combust. Inst. 28 (1) (2000) 59–65.

[24] S.P. Ahmed, Studies of Turbulent Burning Rates and Flame Structures Using 3D Optical Measurement Techniques (Ph.D. thesis), University of Leeds, 2019.

[25] G. Taubin, Curve and surface smoothing without shrinkage, in: Proceedings of IEEE International Conference on Computer Vision, IEEE, 1995, pp. 852–857.

[26] B.J.A. Thorne, Development of a 3D Laser Imaging System and its Application in Studies of Turbulent Flame Structure (Ph.D. thesis), University of Leeds, 2017.

[27] A.N. Lipatnikov, J. Chomiak, Comment on "Turbulent burning velocity, burned gas distribution, and associated flame surface definition" -D. Bradley, MZ Haq, RA Hicks, T. Kitagawa, M. Lawes, CGW Sheppard, R. Woolley, Combust. Flame 133 (2003) 415, Combust. Flame 1 (2004) 261–263.

[28] S. Rusinkiewicz, Estimating curvatures and their derivatives on triangle meshes, in: Proceedings. 2nd International Symposium on 3D Data Processing, Visualization and Transmission, 2004, 3DPVT 2004, IEEE, 2004, pp. 486–493.

[29] M. Meyer, M. Desbrun, P. Schröder, A.H. Barr, Discrete differential-geometry operators for triangulated 2-manifolds, in: Visualization and Mathematics III, Springer, 2003, pp. 35–57.

[30] D.G. Goodwin, R.L. Speth, H.K. Moffat, B.W. Weber, Cantera: an object-oriented software toolkit for chemical kinetics, thermodynamics, and transport processes, 2021, Version 2.5.1.

[31] G.P. Smith, D.M. Golden, M. Frenklach, N.W. Moriarty, B. Eiteneer, M. Goldenberg, C.T. Bowman, R.K. Hanson, S. Song, W.C. Gardiner Jr., et al., GRI 3.0 Mechanism, Gas Research Institute, 1999.

[32] F. Halter, C. Chauveau, I. Gökalp, D. Veynante, Analysis of flame surface density measurements in turbulent premixed combustion, Combust. Flame 156 (2009) 657–664.

[33] Z. Zhou, Y. Shoshin, F.E. Hernández-Pérez, J.A. van Oijen, L.P. de Goey, Effect of Lewis number on ball-like lean limit flames, Combust. Flame 188 (2018) 77–89.

[34] D. Bradley, C. Sheppart, R. Woolley, D. Greenhalgh, R. Lockett, The development and structure of flame instabilities and cellularity at low Markstein numbers in explosions, Combust. Flame 122 (1–2) (2000) 195–209.

[35] A. Trouvé, T. Poinsot, The evolution equation for the flame surface density in turbulent premixed combustion, J. Fluid Mech. 278 (1994) 1–31.

[36] D. Veynante, J. Piana, J. Duclos, C. Martel, Experimental analysis of flame surface density models for premixed turbulent combustion, Symp. (Int.) Combust. 26 (1996) 413–420.